ChemCatChem

ChemCatChem
Chemistry Europe
European Chemical Societies Publishing

RESEARCH ARTICLE OPEN ACCESS

Modeling of the Methanation Reaction Under Transient Conditions Based on Spatially and Temporally Resolved Operando DRIFTS Data

David Kellermann[1] | Timo Engl[2] | Lukas Lipinski[1] | Roland Dittmeyer[2] | Michael Rubin[2] | Hannsjörg Freund[1]

[1]Institute of Reaction Engineering and Catalysis (REC), TU Dortmund University, Dortmund, Germany | [2]Institute For Micro Process Engineering (IMVT), Karlsruhe Institute of Technology (KIT), Eggenstein-Leopoldshafen, Germany

Correspondence: Hannsjörg Freund (hannsjoerg.freund@tu-dortmund.de)

Received: 31 October 2025 | **Revised:** 21 April 2026 | **Accepted:** 22 April 2026

Keywords: CO_2 methanation | heterogeneous catalysis | kinetic modeling | operando DRIFTS | reaction mechanism

ABSTRACT

In the transient operation of decentralized power-to-gas plants, catalyst dynamics can play a crucial role. For the improved description of such dynamics, the *rate affecting step* (RAS) approach was developed by Langer et al. Following this approach, in this work, a kinetic model for the methanation reaction over an industrial Ni/Al_2O_3 methanation catalyst was derived and parametrized using data from a unique laboratory reactor. This reactor setup was specifically developed and built within the priority program SPP2080 "DynaKat" (German Research Foundation), aiming to collect spatially and temporally resolved DRIFTS absorbance data of catalyst surface intermediates. This data was used to tune the performance of the derived RAS model and to evaluate its prediction accuracy. For most scenarios investigated, also including sudden variations in feed composition such as H_2 and CO_2 drop out/in scenarios and variations in space velocity, the model describes the changes in surface coverage of formate and adsorbed CO reasonably well. Thus, in this work, a first-of-its-kind methodology for including *operando* DRIFTS data in a parameter estimation routine for a reaction kinetic model is presented. The results are promising and prove the feasibility of this approach, thereby illustrating future opportunities for its use in high-fidelity reaction kinetic modeling.

1 | Introduction

To limit the extent of the climate change, it is vital to reduce CO_2 emissions. As a consequence, the primary source of energy in the future energy system must be covered in particular by renewable electricity, thus wind power and photovoltaic capacities need to be further increased rapidly worldwide. These, however, are by nature fluctuating sources of energy, which makes it necessary to develop storage solutions for electricity. While batteries offer a good solution for short- and mid-term storage, for long-term storage and distribution of larger amounts of energy, converting electrical energy into chemical energy is a promising approach, also known as power-to-X. One concept is the well-known power-to-gas process, where electricity is used to produce hydrogen via water electrolysis. The hydrogen is further converted together with CO_2 of non-fossil origin to methane. This synthetic natural gas can then be added to the natural gas grid with its large capacity and well-developed distribution network [1]. The process itself is fairly established, especially for stationary operation, see, for example, technology reviews by Rönsch et al. [2] and Tommasi et al. [3].

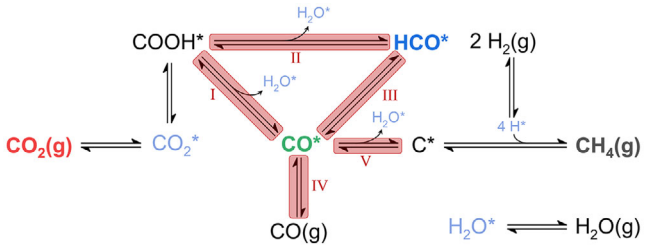

FIGURE 1 | Schematic representation of the RAS-5 model. In this case, five reactions were defined as rate-affecting steps (RAS). Adsorbed species are marked with an asterisk (*) and gaseous species with (g). The RAS are marked in red, the most abundant surface species (MASI) in equilibrium in light blue, and the dynamic surface coverages according to their later used color code. Some reactions and reactants are omitted in the figure for improved readability. Figure adapted from Schmider et al. [22].

However, in the power-to-X context with its fluctuating feed conditions, stationary operation is only possible when applying buffer solutions for electricity (batteries) or reactants (CO_2 resp. H_2 buffer tanks). Gorre et al. [4] showed that expensive hydrogen buffer tanks should be avoided, and as a consequence, it is advantageous to operate the methanation reactor in dynamic operation mode within a certain load range. Previous work from Fischer et al. [5] has shown that process modeling and simulation offer great opportunities for predicting reactor behavior in transient operation and for deriving optimal operation policies. Most studies use kinetic models that follow a classical Langmuir-Hinshelwood-Hougen-Watson (LHHW) approach. A review on kinetic models was published by Rönsch et al. [6] and Tommasi et al. [3]. Frequently used kinetic models are, for example, those of Koschany et al. [7] and Xu and Froment [8]. All of these models are derived using the quasi-equilibrium assumption for the composition on the catalyst surface. This makes these kinetic models less suitable for describing dynamic effects that occur, e.g., during switching of the H_2/CO_2 ratio or complete drop outs. The importance of such effects was reported in experimental studies by Kreitz et al. [9], Friedland et al. [10–12], and Meyer et al. [13–15] for the CO methanation. As a consequence, a new class of kinetic models is necessary, as recently pointed out in the work of Langer et al. [1].

The new concept of rate affecting step (RAS) models proposed by Langer et al. [1] offers a good combination of precise prediction of dynamic reactor operation as well as limited complexity to make parametrization using experimental data possible. A general comparison of the performance of RAS and LHHW models is provided in Langer et al. [1]. The authors compare the number of parameters, computing time, and prediction accuracy of an RAS and an LHHW model with a microkinetic elementary step model as a benchmark, concluding that, while the computing time is only slightly higher, the prediction accuracy of dynamic effects is significantly increased. Nevertheless, compared to LHHW models, more data and knowledge regarding the processes on the catalyst surface is necessary. To fill this gap and provide this knowledge and data, a channel-type laboratory reactor with optical access to the catalyst surface and sample taps for gas phase analysis has been developed and set up within the priority program "DynaCat" (SPP2080), funded by the German Research Foundation (DFG) within the project "Tackling irreversible catalyst deactivation: knowledge-driven design and operation of dynamic responsive methanation catalysts". While channel-type reactors for gathering spatially resolved concentration profiles were already described in literature (see e.g., [16–18]), the reactor used in this study is able to combine *operando* DRIFTS (diffuse reflectance infrared Fourier transform spectroscopy) with online gas phase analysis (gas chromatography, GC). This allows determining both, surface species including their change during dynamic operation as a function of time and location and the concentration profile along the reactor length in the gas bulk phase. A detailed description of the spatially resolved DRIFTS (SRD) reactor is given below and described further in Engl et al. [19] and Weber et al. [20]. A similar investigation, but with an external DRIFTS cell, is presented in a recent publication by Sichert et al. [21].

2 | Kinetic Model, Material and Methods

2.1 | Kinetic Modeling of the Methanation Reaction

As a basis for the kinetic modeling, the microkinetic elementary step model according to Schmider et al. [22] was used. Starting from this model, consisting of a set of overall 42 elementary reactions and 14 surface species, an RAS model of reduced complexity was derived. Taking into account the mechanistic knowledge from previous works [1, 22], the five RAS shown in Figure 1 are used for the model (hereinafter referred to as the RAS-5 model).

In the reaction scheme depicted in Figure 1, the reverse water gas shift (RWGS) reaction can take place via two routes. Surface bicarbonate (COOH*) is in quasi-equilibrium with adsorbed CO_2 and H_2 and reacts to Ni-CO (CO*) and OH* via dissociation. In the RAS-5 model, the second path via formate (HCO*) is also considered since recent literature [22], and own findings indicate that formate is an important surface intermediate. Furthermore, this allows additional degrees of freedom for modeling, also considering the possibility of a change in the main reaction path dependent on the reaction conditions. At this point, it should be noted that this represents only one possible mechanism that is suitable for describing dynamic CO_2 methanation. This reaction scheme represents major reactions derived from DRIFTS and Schmider et al. [22]. The rate equations were derived thoroughly from the rate equations of the elementary steps. The derivation is described in detail in Langer et al. [1]. The resulting reaction rates for the RAS model are:

$$r_{\mathrm{I}} = k_{\mathrm{I}} \cdot \Theta_{\mathrm{CO_2}} \cdot \Theta_{\mathrm{H}} - \frac{k_{\mathrm{I}}}{K_{\mathrm{I}}} \frac{\Theta_{\mathrm{H_2O}} \cdot \Theta_{\mathrm{CO}}}{\Theta_{\mathrm{H}}} \Theta^{*} \tag{1}$$

$$r_{\mathrm{II}} = k_{\mathrm{II}} \cdot \Theta_{\mathrm{CO_2}} \cdot \Theta_{\mathrm{H}}^{2} \cdot \frac{1}{\Theta^{*}} - \frac{k_{\mathrm{II}}}{K_{\mathrm{II}}} \cdot \frac{\Theta_{\mathrm{HCO}} \Theta_{\mathrm{H_2O}}}{\Theta_{\mathrm{H}}} \cdot \Theta^{*} \tag{2}$$

$$r_{\mathrm{III}} = k_{\mathrm{III}} \cdot \Theta_{\mathrm{HCO}} \cdot \Theta^{*} - \frac{k_{\mathrm{III}}}{K_{\mathrm{III}}} \cdot \Theta_{\mathrm{CO}} \cdot \Theta_{\mathrm{H}} \tag{3}$$

$$r_{\mathrm{IV}} = k_{\mathrm{IV}} \cdot p_{\mathrm{CO}} \cdot \Theta^{*} - \frac{k_{\mathrm{IV}}}{K_{\mathrm{CO,ads}}} \cdot \Theta_{\mathrm{CO}} \tag{4}$$

$$r_V = k_V \cdot \Theta_{CO} \cdot \Theta_H - \frac{k_V}{K_V} \cdot \frac{p_{CH_4} \Theta_{H_2O}}{\Theta_H^5} \cdot \Theta^{*6} \quad (5)$$

with r_j being the reaction rate of the surface reaction j, k_j being the reaction rate constant, K_j the equilibrium constant and Θ_i the surface coverage of the respective surface species i. The temperature dependency of the reaction rate and equilibrium constants is calculated using a reparametrized Arrhenius and van't Hoff approach.

$$k_j = k_{j,ref} \cdot \exp\left(-\frac{E_{A,j}}{R}\left(\frac{1}{T} - \frac{1}{T_{ref}}\right)\right) \cdot \exp\left(\frac{\epsilon_{CO}\theta_{CO}}{R \cdot T}\right) \quad (6)$$

$$K_{j/i} = K_{j/i,ref} \cdot \exp\left(-\frac{\Delta H_j}{R}\left(\frac{1}{T} - \frac{1}{T_{ref}}\right)\right) \quad (7)$$

with the activation energy, $E_{A,j}$ and the enthalpy of adsorption, ΔH_j, the universal gas constant, R, and the temperature, T. The reference temperature T_{ref} should be close to the center of the investigated temperature range (250°C–400°C). Here, it was set to the next higher investigated temperature because the experimental data at higher temperatures is less prone to outliers. The surface coverages of CO_2, H, and H_2O are calculated using the quasi-equilibrium assumption:

$$\Theta_H = \sqrt{K_{ads,H_2} \cdot p_{H_2}} \cdot \Theta^* \quad (8)$$

$$\Theta_{H_2O} = K_{ads,H_2O} \cdot p_{H_2O} \cdot \Theta^* \quad (9)$$

$$\Theta_{CO_2} = K_{ads,CO_2} \cdot p_{CO_2} \cdot \Theta^* \quad (10)$$

with $K_{ads,i}$ being the adsorption constant and p_i the partial pressure of the respective gas phase species. Θ_* is the fraction of free surface sites. The coverages of the dynamic surface intermediates CO* and HCO* are calculated using the surface balances for these species:

$$\Gamma_{Ni}\frac{d\Theta_{CO}}{dt} = r_I + r_{III} + r_{IV} - r_V \quad (11)$$

$$\Gamma_{Ni}\frac{d\Theta_{HCO}}{dt} = r_{II} - r_{III} \quad (12)$$

where $\Gamma_{Ni} = 2.6 \cdot 10^{-5}$ mol m^{-2} [22] is the overall number of surface sites and r_j the reaction rates of the RAS in which the surface intermediate is consumed or produced. The free surface sites Θ* are calculated using the surface balance with all MASI species:

$$\Theta^* = 1 - \Theta_{CO_2} - \Theta_{CO} - \Theta_H - \Theta_{H_2O} - \Theta_{HCO} \quad (13)$$

Following the procedure of Langer et al. [19], the thermodynamic consistency is sustained using the following additional equations, considering also the second path for the RWGS reaction:

$$K_{II} = K_{eq,RWGS}\frac{K_{IV}K_{ads,H_2O}}{K_{III}K_{ads,H_2}K_{ads,CO_2}} \quad (14)$$

$$K_I = K_{II}K_{III} \quad (15)$$

$$K_V = \frac{K_{ads,H_2O}}{K_{IV}K_{ads,H_2}^3}K_{eq,COMeth} \quad (16)$$

The equilibrium constants of the reactions were calculated using the Shomate equations and parameters from the NIST chemistry webbook [23]. Lastly, the catalyst surface is coupled using the catalyst mass specific rates of production or depletion R_i for the gas phase species. For this, it needs to be considered in which RAS the gas phase species take part.

$$R_{CO_2} = S_{Ni} \cdot (-r_I - r_{II}) \quad (17)$$

$$R_{CO} = S_{Ni} \cdot (-r_{IV}) \quad (18)$$

$$R_{H_2} = S_{Ni} \cdot (-r_I - 1.5r_{II} + 0.5r_{III} - 3r_V) \quad (19)$$

$$R_{H_2O} = S_{Ni} \cdot (r_I + r_{II} + r_V) \quad (20)$$

$$R_{CH_4} = S_{Ni} \cdot (r_V) \quad (21)$$

with the specific nickel surface area of the catalyst, S_{Ni}.

2.2 | SRD Reactor, Analysis Methods, and Experimental Operating Conditions

The reactor used for the catalytic experiments is a channel-type reactor with optical access and taps for gas phase sampling. The key characteristics are described in the following, for a more detailed description the reader is kindly referred to previous publications [19, 20, 24]. The reaction chamber is divided into five reaction zones (RZ), each hosting one microstructured foil with the dimensions of 22 × 24 mm coated with the catalyst. The catalyst used is an industrial Ni/Al_2O_3 catalyst (referred to as SPP2080-IMRC, where IMRC stands for industrial methanation reference catalyst) with a particle size of <3 µm. The catalyst consists of 8.6 wt.-% nickel supported on aluminum oxide and has been extensively studied in literature [19, 25, 26]. The coating of the microstructured foils with the SPP2080-IMRC has been described in detail in Engl et al. [19]. The present study focuses on its experimental characterization using the SRD reactor. Five catalyst plates were prepared via screen printing ($m_{catalyst}$ = 20.8, 14.4, 19.8, 20.6, 19.6 mg for RZ1 to RZ5, m_{total} = 95.2 mg) and placed in the reactor. The catalyst was in-situ reduced in 50 vol. % H_2 in N_2 for 8 h at 400°C and atmospheric pressure at a flow rate of 300 mL_N min^{-1}. After reduction, the reactor was purged with pure N_2 (99.999 vol. %) and pressurized to 5 bar(a). Between each catalyst foil a sampling port allows for spatially resolved sampling of the gas phase to measure a concentration profile along the reactor coordinate. A CaF_2 window on top of the reactor allows light, especially infrared radiation, to enter and leave the reactor allowing for spatially resolved DRIFTS analysis. As a radiation source, an IR cube FT-IR OEM spectrometer with a resolution of 4 cm^{-1} from Bruker Optics was used to generate IR radiation in a wave number range from 4000 to 1150 cm^{-1} (liquid N_2 cooled Mercury Cadmium Telluride (MCT) detector). In this range most of the adsorbed species such as Ni-CO (2061 cm^{-1} [27, 28]), bicarbonate (1647, 1442, and 1228 cm^{-1} [27, 28]) and formate (2900, 1293, and 1373 cm^{-1} [27, 29]) and also some of the gaseous species such as CH_4 (3014 and 1305 cm^{-1} [27, 29]) and CO_2 (2360 and 2343 cm^{-1} [27, 28]) absorb light.

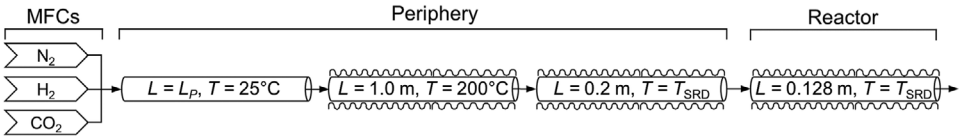

FIGURE 2 | Schematic depiction of the plant setup. Downstream of the mass flow controllers (MFCs) is unheated piping and 1.0 m of heated piping with an inner diameter of 4 mm. The length of the unheated pipe is determined from measurements, lumping unknown volumes. The preheated gas is then fed into the reactor where it is further heated to the reaction temperature before it reaches the catalyst. This heating is simulated via an ideal heat exchanger.

Before the analysis of the catalyst under methanation conditions, background spectra were measured for each temperature and RZ to subtract influences of the mirrors, spectrometer and other device properties from the sample spectrum, allowing for only investigating the effects of species involved in the methanation reaction. For the acquisition of the background spectra, a slightly reducing atmosphere is used (10 vol. % H_2 in N_2) at 5 bar(a) pressure. The spectrum is averaged over 40 single spectra to minimize noise. For the sample spectra, a resolution of 4 s averaged over four spectra is used, optimizing the trade-off between high resolution and a minimum of noise in the resulting spectrum.

For three reaction zones (RZ1 at a dimensionless reactor length of 0.1, RZ3 at a dimensionless reactor length of 0.5 and RZ5 at a dimensionless reactor length of 0.9) and at seven temperatures between 250°C and 400°C in steps of 25 K, five different experiments in temporal resolution were carried out. The pressure was 5 bar(a), a stoichiometric feed ratio of CO_2:H_2 of 1:4 was applied at a space velocity (SV) of 4.6 $mL_N\ min^{-1}\ mg_{cat}{}^{-1}$ with a dilution with N_2 of 50 vol. %. At first, a CO_2 drop out and successive drop in as well as an H_2 drop out and drop in were carried out. The gas which was dropped out was completely replaced by the same amount of N_2 to retain a constant volume flow. In a next set of experiments, the feed composition was varied from 1:4 to 1:1 and back as well as 1:4 to 1:8 and back to investigate the effects of different gas concentrations on the catalyst and its adsorbed species. At last, the SV was varied from 4.6 to 1.0 $mL_N\ min^{-1}\ mg_{cat}{}^{-1}$ and back to investigate the influence of change in conversion on the adsorbed species.

2.3 | Reconciliation of Experimental Data and Parameter Estimation

DRIFTS data only yield absorbance data for each species; the corresponding partial pressures need to be calculated from reference gas chromatograph (GC) measurements. For this, for every state which right before or at the very end of a drop in resp. drop out experiment, gas phase composition was measured at all tap positions and at the reactor outlet, resulting in 28 experiments with five datapoints each for every gas phase component except H_2O. The data reconciliation procedure also used in Langer and Freund [30] is applied. For this, the extent of reaction ξ_j is introduced for the two key reactions, the RWGS and the CO_2 methanation reaction and the local molar balance can be set up for each tap position:

$$\hat{\dot{n}}_i = \dot{n}_{i,\mathrm{in}} + \sum_{j=1}^{N_R} \nu_{i,j} \cdot \hat{\dot{\xi}}_j \tag{22}$$

With the observed extent of reaction $\hat{\dot{\xi}}_j$ and the local molar flow $\hat{\dot{n}}_i$, the molar flow at the reactor inlet $\dot{n}_{i,\mathrm{in}}$, and the stoichiometric coefficients $\nu_{i,j}$. Using the definition of the molar fractions of the measured components:

$$\hat{x}_i = \frac{\hat{\dot{n}}_i}{\sum_k^{N_{GC}} \hat{\dot{n}}_k} \tag{23}$$

where N_{GC} is the number of components measured by the GC and i, k being these components, the weighted residual of squares ($wRSS$) can then be calculated as follows:

$$wRSS = \sum_i^{N_{GC}} \frac{\left(x_{i,\mathrm{GC}} - \hat{x}_{i,\mathrm{GC}}\right)^2}{\sigma_i^2} \tag{24}$$

where $x_{i,GC}$ are the actually measured molar fractions without water and σ_i^2 is the variance of the measurements which can be estimated using a linear variance model. The $wRSS$ is then minimized using the sequential least squares programming (SLSQP) solver from scipy in Python, resulting in a set of ten datapoints for each steady state experiment. To link the steady-state gas phase data to the dynamic experiments, the gas phase concentrations in the center of the reaction zones are required. Since the difference in conversion is comparatively low between the two tap positions, the concentration can be approximated using linear interpolation between these tap positions. The molar fractions in the transition region of the dynamic experiments are calculated by correlating the measured absorbances to the steady-state GC measurements at the beginning and the end of each experiment and their corresponding absorbances. To mitigate the effect of noise in the DRIFTS measurement, for each steady state, the first and last five datapoints are averaged and correlated to the GC measurement. For drop in or drop out experiments, the gas phase compositions are assumed to be ideal, e.g., the CO_2 molar fraction is set to 10 or 0 %, and the H_2 fraction to 40 or 0 %. To use the measured absorbance values A_i for the parameter estimation, a correlation variable b_i is introduced, which links the DRIFTS signal to the surface coverage:

$$A_i = b_i \cdot \theta_i \tag{25}$$

with $i \in$ [HCO*, CO*]. Since the DRIFTS signal strongly correlates with temperature, the variable b_i needs to be estimated for every investigated temperature and species.

The parameter estimation is conducted iteratively. In a first step, the kinetic model is parametrized using the data from steady-state experiments. In a second step, the parameters are tuned using the data from the dynamic kinetic experiments, and a first guess

for parameter b_i is determined. To ensure the prediction accuracy in the steady state, the kinetic model is then again fitted to the steady-state data. This is repeated in an iterative approach until the desired model accuracy is achieved.

2.4 | Modeling of the Laboratory Plant

For an accurate description of transient experiments in the laboratory setup, not only the reactor itself but also the relevant periphery has to be taken into account. The setup is depicted in Figure 2. The periphery, consisting of heated and unheated pipes, results in dispersion effects which superimpose the dynamic effects in the reactor. To be able to model the kinetics of the catalyst surface, dispersive effects in the laboratory plant need to be identified. The length L_P of the first unheated (ambient temperature, 25°C) pipe is determined once in a first step on the basis of the residence time in the dynamic measurements, to also account for any unknown volumes in the periphery. The length and temperature of the second, heated pipe is in agreement to the laboratory setup, that is, 1 m and 200°C. The pre-heating zone in the SRD reactor is also modeled as a pipe with a length of 20 cm and a constant temperature equal to the reaction temperature (250°C–400°C). For the discretization, the backward finite differences (BFDM) scheme was used. The unheated pipe was discretized with 250, the heated pipe with 50, the heat exchanger with 20, and the reactor with 100 elements.

2.4.1 | Balance Equations

In the modeling process of the SRD reactor, assumptions were made as described in the following. Since the pressure for the simulations and experiments is below 10 bar, the ideal gas law is applied as the equation of state. The pressure is assumed to be constant along the reactor axis (i.e., the pressure drop is negligible). No internal mass transport influences need to be considered since the catalyst layer is very thin (i.e., approx. 40 µm). External mass transport limitations were excluded based on previous investigations. Results from the laboratory reactor indicate that the reactor is operated isothermally. The width of the channel is large compared to the height, so the effect of the outer walls is assumed to be negligible. Consequently, gradients in this direction are not considered. In our previous work [24], we have shown by detailed CFD simulations that the concentration gradients along the channel height are also negligible. Further investigations on the flow field in the SRD reactor indicated a strongly laminar flow field, making it necessary to take axial dispersion into account when using a 1D model.

2.4.2 | Reactor Model With Axial Dispersion

For the derivation of the mathematical reactor model, only gradients in the axial direction are considered, and the reactor is modeled using a 1D axial dispersion model. This model is commonly used in literature for the simplified description of reactors with laminar flow [31]. The resulting material balance expressed in the form of concentrations is:

$$\frac{\partial c_i}{\partial t} = -\frac{\partial}{\partial z}\left(c_i \bar{v}_z\right) + \frac{\partial}{\partial z}\left(D_{i,\mathrm{ax}} \frac{\partial c_i}{\partial z}\right) + \bar{\rho}_{\mathrm{cat}} \cdot R_{\mathrm{i}} \tag{26}$$

where $\bar{v}_z$ is the superficial velocity, $D_{i,ax}$ is the axial dispersion coefficient, and $\bar{\rho}_{\mathrm{cat}}$ is the catalyst density in relation to the total reactor volume. As boundary conditions regarding the axial domain of the gas phase for the 1D model, Dirichlet and Neumann conditions are implemented:

$$c_i\Big|_{z=0} = c_{i,\mathrm{in}}, \left.\frac{\partial c_i}{\partial z}\right|_{z=L} = 0 \tag{27}$$

with L being the reactor length.

2.4.3 | Modeling of Dispersion

For the 1D model, the axial dispersion coefficient is calculated using the model of Taylor and Aris for a rectangular flow channel [31]:

$$\frac{D_{i,ax}}{D_{i,\mathrm{mix}}} = 1 + \frac{\mathrm{Pe}_{i,\mathrm{m}}^2}{210} \tag{28}$$

For modeling the dispersion within the periphery, the constant 210 is altered to 192 for the flow in the tubular pipes of the periphery, with the molecular Peclet number:

$$\mathrm{Pe}_{i,\mathrm{m}} = \frac{\bar{v}_z\, H}{D_{i,\mathrm{mix}}} \tag{29}$$

with the height of the reaction channel, H. Furthermore, the dynamic viscosity and the thermal conductivity of the pure components are calculated using the method of Kleiber and Joh [32]. The mixing rules of Wilke [33] were used to estimate the properties for the multicomponent gas phase. The dynamic modeling of the laboratory plant and the parameter estimation was conducted using state-of-the-art solvers in gProms process.

Details on the simulation of the step experiments are given in the Supporting Information.

3 | Results and Discussion

3.1 | DRIFTS Data of the Dynamically Operated Methanation

In order to gain insights into the type and amount of surface species adsorbed on the catalyst during the methanation reaction, temporally and spatially resolved DRIFTS was carried out as outlined in section 2.2 on a large set of parameter variations. Special focus was laid on the investigation of effects during step-changes of relevant process conditions, namely CO_2 drop out and drop in, H_2 drop out and drop in, CO_2:H_2 feed ratio variation (1:4 to 1:1 and vice versa as well as 1:4 to 1:8 and vice versa) and SV variation (1.0 to 4.6 $mL_N\ min^{-1}\ mg_{cat}^{-1}$ and vice versa). All these variations were investigated at different reaction temperatures (250°C–400°C in 25 K increments) and positions along the reaction coordinate (reaction zones RZ1, RZ3, and RZ5). In general, step changes were only applied to one specific parameter while keeping all others constant. A large number of experiments, collected from temporally (resolution: 4 s) and spatially resolved data resulting from the broad set of variations (10 step changes x 7 different

reaction temperatures x 3 reaction zones equals 210 data sets out of 105 individual experiments) served as a basis for modeling the gas phase concentration and, above all, the surface species. In the following, a representative set of experiments is described in more detail. Figure 3 shows the time-resolved, normalized absorbances of the surface and gas phase species detected in RZ5 at 350°C, 5 bar(a), and SV of 4.6 $mL_N\ min^{-1}\ mg_{cat}^{-1}$ of the different step change experiments (see Supporting Information for exemplary data on temperature variation and different reaction zones). The sudden change in the accordant varied process parameter was always initiated at the arbitrary timestamp "30 s" depicted in Figure 3a–j. However, the resulting changes in the DRIFTS signal could only be observed with a certain delay (approx. 30 s) caused by the imposed step-change through the plant peripherals (see also Section 2.2 for details).

After CO_2 drop out (Figure 3a), the concentration of CO_2 in the gas phase readily decreases and consequently approaches zero. As a result, the absorbances of the intermediates formate and Ni-CO likewise decrease, as these species are no longer formed from CO_2 (paths II and III in Figure 1), but rather react with the H_2 that is still being fed into the reactor to form CH_4, which is indicated by the less pronounced decrease in CH_4 signal even though CO_2 feed is not available anymore. Eventually, carbonyl from Ni-CO vanishes completely from the surface of the catalyst while, in contrast, formate to some extent remains present even after several minutes after the CO_2 drop out (approximately 20% of its original value), indicating a strong chemisorption on the catalyst surface. These observations are in line with the phenomena reported by Wang et al. [34]. After CO_2 drop in (Figure 3b), the initial states are reached again. However, in contrast to the CO_2 drop out, after drop in all species discussed reach the initial state after just a few seconds following with similar rate. The absorbances of formate and Ni-CO increase respectively reappear as CO_2 is once again available as a reactant.

After H_2 drop out (Figure 3c), the CH_4 concentration readily drops to zero, as there is no longer any H_2 available for the hydrogenation of the carbon species (path V in Figure 1), supporting the proposed mechanism during CO_2 drop out. With the absence of H_2, the absorbance for gaseous CO_2 increases, as it is no longer converted into CH_4, thereby increasing the concentration in the gas phase. The absorbance of Ni-CO strongly increases as its further reaction (path V in Figure 1) is hindered due to lack in H_2 as a reactant. Formate, on the other hand, does show some decrease, as the further reaction, i.e., the dissociation of formate to Ni-CO (path III in Figure 1), can also take place without H_2. As soon as H_2 is fed again (Figure 3d), the species readily retain their initial state following the trends to be expected, namely the restart of the conversion of CO_2 to CH_4 with the accompanying slight decrease resp. increase in the DRIFTS signal, the hydrogenation of Ni-CO to CH_4 (decrease of Ni-CO signal), and the formation of formate due to the re-availability of hydrogen. The normalized absorbance of CO_2 shows a small peak during the switching phase, which results in lower values due to the normalization calculation to the maximum value. As the absorbances without the normalization show (see Figure S4), the original values are obtained after the switch back to methanation conditions.

The variation in the feed composition has a major influence on the methanation reaction. By changing the feed ratios (CO_2:H_2) at the reactor inlet, the adsorbed species adapt to the respective new partial pressures. In Figure 3e it becomes clear that as the inlet concentration of CO_2 increases (step change from stoichiometric CO_2:H_2 = 1:4 to 1:1), its relative content in the reactor also increases. At the same time, the absorbances of the adsorbed species formate and Ni-CO also increase, as a high CO_2 partial pressure favors the adsorption resp. formation of these species. With the deviation from the optimal stoichiometric inlet conditions, the CH_4 concentration decreases slightly, as there is no longer sufficient H_2 available to further convert the intermediates. With the step change back to an initial, stoichiometric ratio of CO_2 to H_2 (Figure 3f), it can be seen that all components retain their original values within a few seconds. During the step change, formate and Ni-CO signals exactly follow that of gaseous $CO_{2,g}$, which is in line with the expectation that the surface coverages of these species are directly dependent on the CO_2 partial pressure.

The time-resolved normalized absorbances of the adsorbed and gas phase species when changing the feed composition from the stoichiometric ratio CO_2:H_2 = 1:4 to a scenario with excess hydrogen (CO_2:H_2 = 1:8) are shown in Figure 3g. Due to the excess of H_2, the concentration of gaseous $CO_{2,g}$ decreases, as not only the share in the feed is decreased, but also more CO_2 is eventually converted to CH_4. This is also evident in the adsorbed species formate and Ni-CO. The absorbances follow that of $CO_{2,g}$, and lose more than half of the signal intensities. When the feed composition is changed back to stoichiometry (Figure 3h), the initial state of all species is readily reached again. The influence of the step change in the feed composition further increases with increasing reaction temperature. In Figures S2 and S3, the time-resolved normalized absorbances of the adsorbed and gas phase species for the step change in feed composition from a stoichiometric to an overstoichiometric ratio are shown for the temperatures from 250°C to 400°C in steps of 25 K at 5 bar(a), a SV of 4.6 $mL_N\ min^{-1}\ mg_{cat}^{-1}$ and a dilution with N_2 of 50 vol. %. At 250°C, no changes in the concentration of the adsorbed species are seen, which changes at 275°C were Ni-CO and formate, start to decrease with overstoichiometric conditions compared to stoichiometric ones. At 400°C, the absorbance of the adsorbed species is decreased by around 50 % due to the maximum change in conversion.

In contrast to the changes of the reaction parameters described above, the SV variation, namely from 4.6 to 1.0 $mL_N\ min^{-1}\ mg_{cat}^{-1}$ and vice versa, does not change the composition of the feed, but rather the total volume flow. Reducing the SV from 4.6 to 1.0 $mL_N\ min^{-1}\ mg_{cat}^{-1}$ (Figure 3i) instantly increases the contact time of the reaction gases with the catalyst, which likewise instantly increases the conversion of CO_2 and H_2 in the kinetically limited reaction, which can be observed by the increase in CH_4 concentration, respectively, the decrease in CO_2 concentration right after the step change was initiated. It should be mentioned that, since the total volume flow decreases by a factor of 4.6 during this variation, the pressure also decreases briefly due to the required readjustment of the pressure regulator, causing an overlaying effect concerning the change of the different species. This, however, stabilizes after around 90 s where the signal of all species approaches a plateau. Among the adsorbed species, formate shows a trend similar to CO_2, as the formation, respectively the adsorption, of formate depends on the partial pressure of CO_2. Ni-CO, meanwhile, remains rather constant

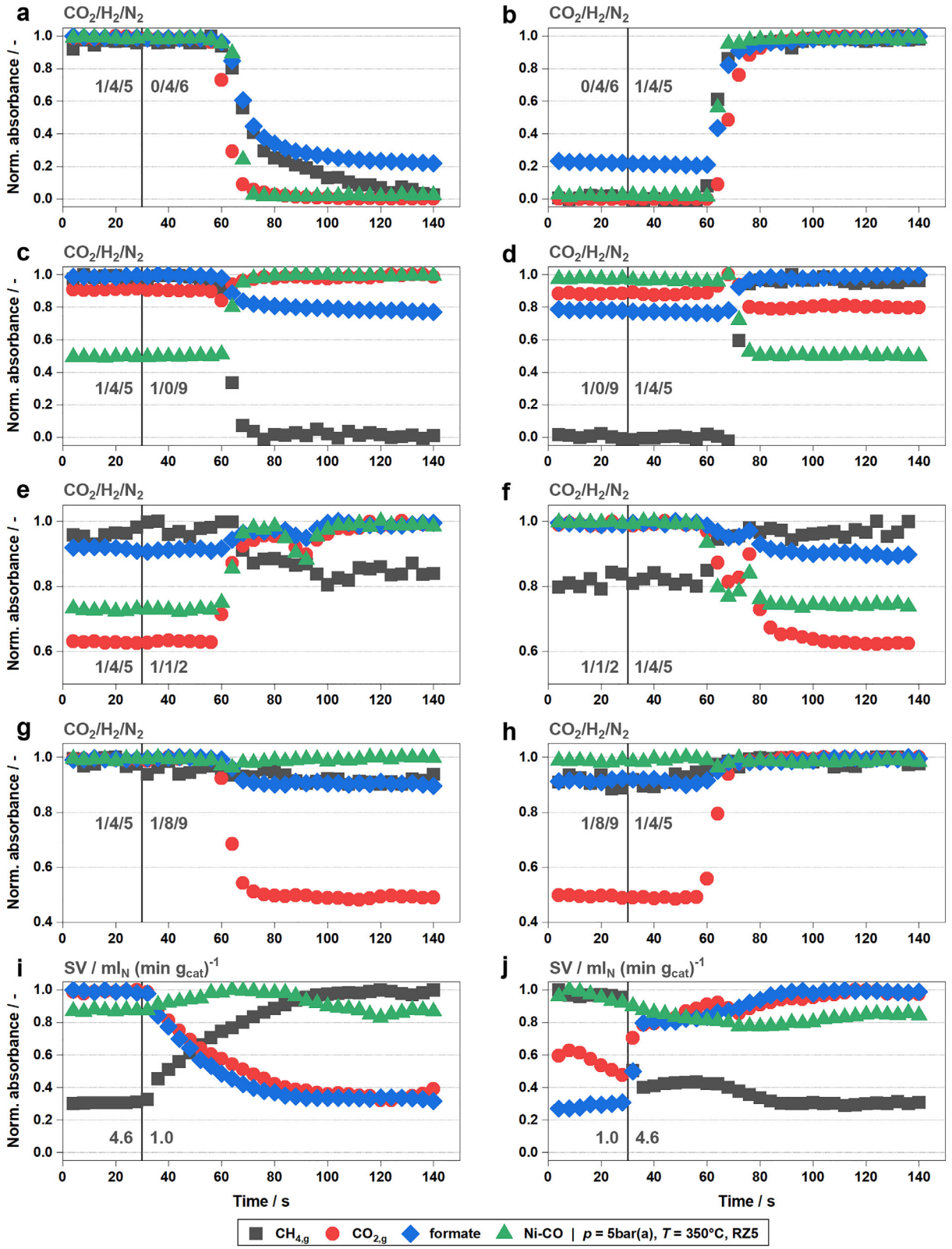

FIGURE 3 | Time resolved representation of the normalized absorption of $CH_{4,g}$ (3014 cm^{-1}), $CO_{2,g}$ (2360 cm^{-1}), formate (1593 cm^{-1}) and Ni-CO (2061 cm^{-1}) in RZ5 at 350°C, 5 bar(a), with a SV of 4.6 ml_N min^{-1} $mg_{cat}{}^{-1}$ for the (a) CO_2 drop out, (b) CO_2 drop in, (c) H_2 drop out, (d) H_2 drop in, (e) variation of the CO_2 to H_2 ratio from 1:4 to 1:1, (f) variation of the CO_2 to H_2 ratio from 1:1 to 1:4, (g) variation of the CO_2 to H_2 ratio from 1:4 to 1:8, (h) variation of the CO_2 to H_2 ratio from 1:8 to 1:4, (i) variation of the SV from 4.6 to 1.0 and (j) variation of the SV from 1.0 to 4.6. Before the drop out and after the drop in, CO_2 and H_2 have a stochiometric feed with a dilution with N_2 of 50 vol. %. During the drop out, CO_2 and H_2 were respectively replaced by the same amount of N_2.

independent of the SV (deviations are assigned to the slight changes in pressure). When increasing the SV again from 1.0 to 4.6 $ml_N\ min^{-1}\ mg_{cat}^{-1}$ (Figure 3j), all species readily adapt to the new volumetric flow rate conditions, that is, all species retain their initial value. Variations in the first approx. 60 s after the step change in SV are again to be assigned to the imposed changes in pressure, as the pressure regulator requires some time to readjust for the new flow rate conditions set. Similar results are seen in every RZ. In Figure S1, the comparison between the temporally resolved experiments for every RZ is shown for 350°C, 5 bar(a) and stoichiometric feed with a dilution with N_2 of 50 vol. %. It is seen that the drop in CO_2 concentration, and therefore formate concentration, is seen in RZ1 since there the reaction rate is highest. In RZ3 and RZ5, Ni-CO stays rather constant while formate follows the trend of CO_2.

3.2 | Modeling of Dynamic Experiments

Before the modeling of the dynamic experiments, the derived kinetic model was parametrized using the steady state data. The results for the parametrization of the RAS-5 and the LHHW model can be found in Tables S1 and S2. The results show that parameters describing the formate route between COOH* and CO* display a high statistical uncertainty. This is to be expected, since only gas phase data was used for parametrization, and this data can, in principle, completely be described via the COOH* to CO* pathway (I). Therefore, it can be concluded that data for surface species, e.g., from DRIFTS, is necessary to determine these parameters with higher statistical significance.

As the next step, the length of the unheated pipe (see explanation in Section 2.4) was approximated during parameter estimation to be 371.2 cm. To investigate the prediction accuracy of the model applied for the dynamic experiments, it was compared to a conventionally derived LHHW model as a reference. This LHHW model was taken from literature [30], modified with a washcoat factor, and reparametrized to match the steady state experimental data of the present work and to allow for a comparative evaluation of both models.

It should be emphasized that for the parameterization of the models, a total of 29,400 data points from 210 experiments were used. However, for further discussion, data of the reaction zone 5 (RZ5) are used, showing the most pronounced effects (see S1 in Supporting Information for exemplary data comparing reaction zones RZ1, RZ3, and RZ5).

3.2.1 | Gas Phase Concentrations

The results of the simulations and results from the experiments (DRIFTS data for the gas phase species) are depicted in Figure 4. The time of the simulated step change varies in some experiments because of the temporal offset correction (see Section 2.4). Both kinetic models describe the experimental data well, and the difference between both models is negligible for the investigated conditions. The reason for these minor deviations can be found in the scale of the experimental setup. While the SRD reactor offers the possibility of collecting a large amount of data, including data on the catalyst surface, it only contains a small amount of catalyst. This prevents the development of strong dynamic effects, as these depend significantly on the available storage capacity—and thus on the catalyst mass. Previous work [1] has shown that especially the combination of high conversion, low temperatures, and high catalyst mass promotes the development of dynamic behavior due to the high storage capacity of the catalyst surface and the comparatively slow surface kinetics. This indicates that the dynamic effects measured are primarily due to residence time effects. This presumption is supported by the characteristic curvature of the CO_2 signal in the drop out experiments, which corresponds to the residence time distribution of a laminar flow reactor. The largest deviation between simulations and experiments was observed for the SV variations (Figure 4i,j). The reason for this can be assigned to the pressure regulator of the laboratory plant, which was not able to instantaneously adjust the pressure when volume flow rates were altered rapidly to higher (increase in SV) or lower (decrease in SV) values. These dynamic effects could not be depicted by the models, as the temporal resolution of the pressure sensor is not sufficiently high, which required the assumption of a constant reaction pressure of 5 bar.

3.2.2 | Surface Coverages and Absorbances

The surface coverages (model) and relative absorbances (measured by DRIFTS) were compared qualitatively (i.e., both normalized from zero to one within the considered range) since the absolute values cannot be deduced from the raw DRIFTS data obtained from the SRD reactor setup. Nevertheless, on a qualitative level, DRIFTS data can be used to quasi-validate the kinetic models and can provide an indication of which reaction paths are the most relevant ones. As shown in Figure 5a,b, the simulation results for the CO_2 drop in and drop out scenarios are in relatively good agreement with the normalized data from DRIFTS, especially for the drop out experiment. Interestingly, the dynamic effects measured by DRIFTS in the drop in experiment seem to be faster, resulting in an increased deviation of the RAS-5 model.

The H_2 drop out/drop in simulations (Figure 5c,d) show formate steadily transitioning to the next steady state condition, fairly matching the experimental data, while for Ni-CO, a surface concentration peak occurs in the simulation not observable in the experiment. The reason for this phenomenon is that when the hydrogen feed stops (Figure 5c), during the transition period, an H_2/CO_2 ratio develops which favors the RWGS reaction, and thus the CO production, which cannot react further to CH_4 since the H_2 concentration is too low. When the H_2 concentration drops even further, also the RWGS reaction cannot take place anymore, and thus surface CO decreases. This effect seems more pronounced for models with a fast response time, explaining why the peak is higher for the LHHW kinetic model. In the experimental data, this highly dynamic effect seems to be leveled out by three different causes: residence time effects, temporal measurement resolution, and the storage effects on the catalyst. In disagreement with the experimental data, both models suggest the Ni-CO level before the H_2 drop in (Figure 5d) to be lower than after the drop in. When considering a longer period of time, however, the experimental data show the same trend as the models. The desorption of the Ni-CO takes up to 25 min to fully

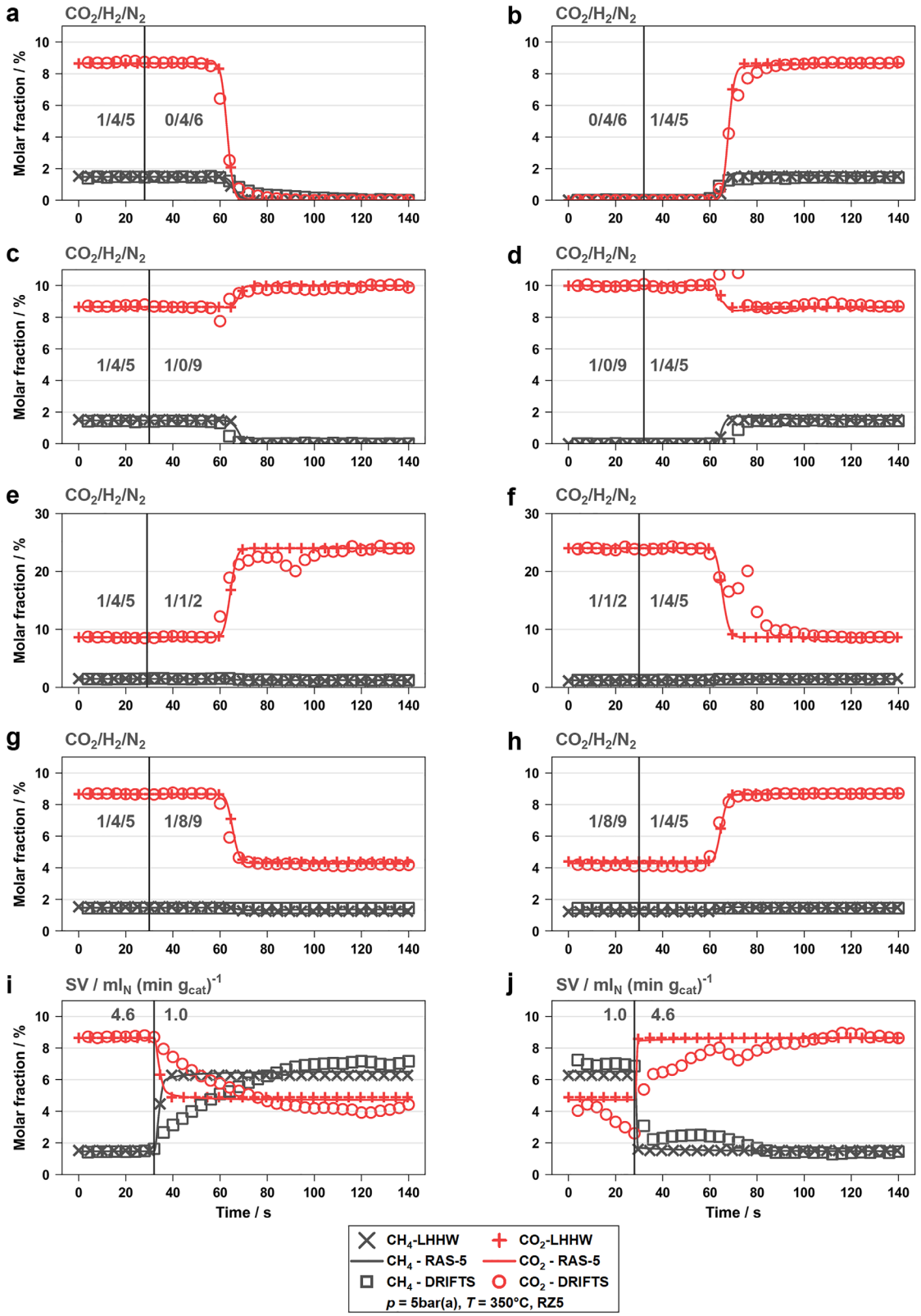

FIGURE 4 | Simulation of the dynamic experiments in RZ5, 5 bar, 350°C with an SV of 4.6 $ml_N\ min^{-1}\ mg_{cat}{}^{-1}$ for (a) CO_2 drop out, (b) CO_2 drop in, (c) H_2 drop out, (d) H_2 drop in, (e) variation of the CO_2 to H_2 ratio from 1:4 to 1:1, (f) variation of the CO_2 to H_2 ratio from 1:1 to 1:4, (g) variation of the CO_2 to H_2 ratio from 1:4 to 1:8, (h) variation of the CO_2 to H_2 ratio from 1:8 to 1:4, (i) variation of the SV from 4.6 to 1.0 and (j) variation of the SV from 1.0 to 4.6 $mL_N\ min^{-1}\ mg_{cat}{}^{-1}$.

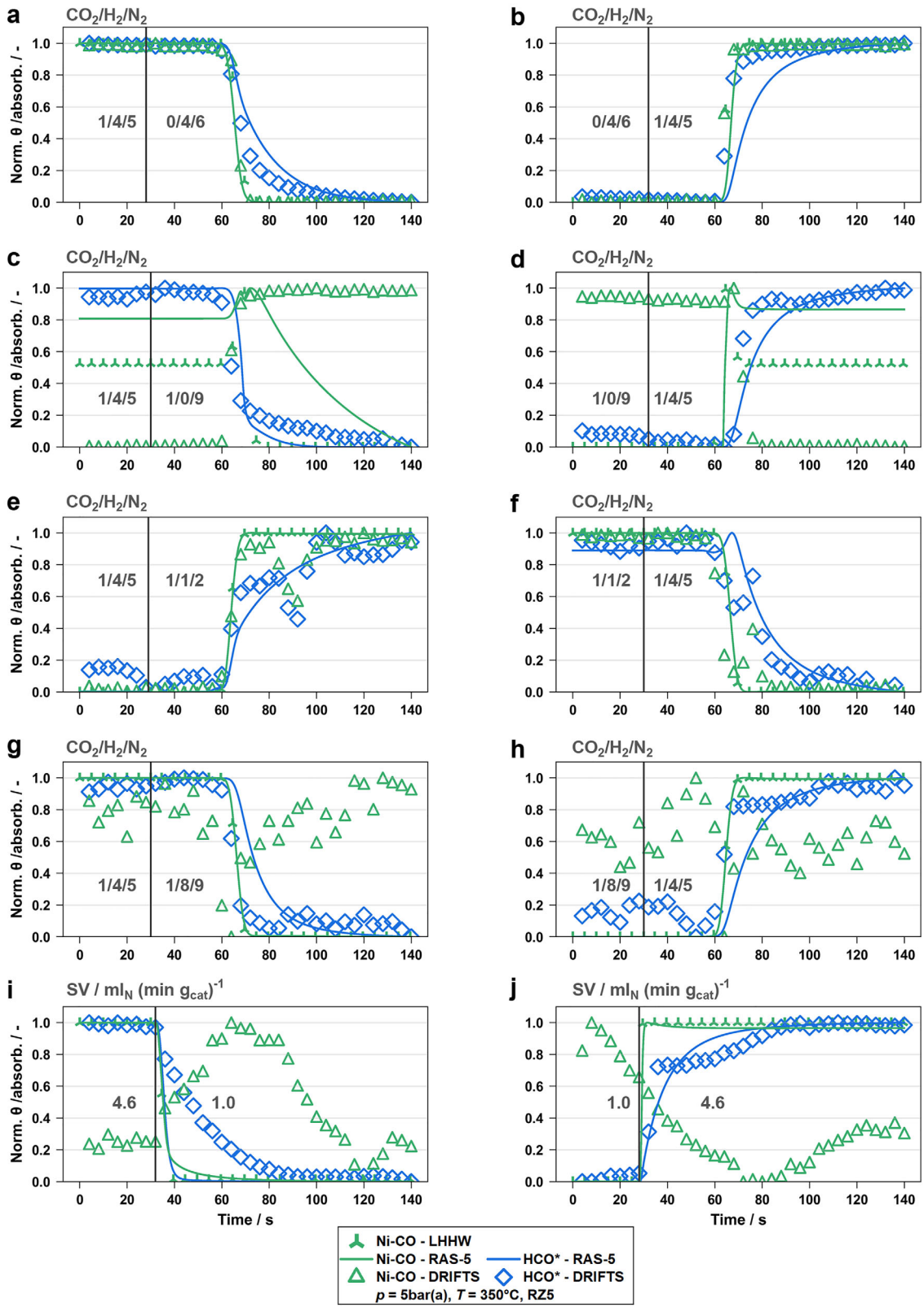

FIGURE 5 | Simulation of the dynamic experiments in RZ5, 5 bar, 350°C, with an SV of 4.6 $mL_N\ min^{-1}\ mg_{cat}{}^{-1}$ for (a) CO_2 drop out, (b) CO_2 drop in, (c) H_2 drop out, (d) H_2 drop in, (e) variation of the CO_2 to H_2 ratio from 1:4 to 1:1, (f) variation of the CO_2 to H_2 ratio from 1:1 to 1:4, (g) variation of the CO_2 to H_2 ratio from 1:4 to 1:8, (h) variation of the CO_2 to H_2 ratio from 1:8 to 1:4, (i) variation of the SV from 4.6 to 1.0 and (j) variation of the SV from 1.0 to 4.6 $mL_N\ min^{-1}\ mg_{cat}{}^{-1}$. Depicted are the normalized absorbances for the experimental data and the surface coverages for the simulated data. Since HCO* is not considered in the LHHW model, its data is missing in the plots. The time of the simulated step change varies in some experiments because of the temporal offset correction (see Section 2.4).

desorb the Ni-CO from the surface. This is shown in Figure S5 in the supporting information for an H_2 drop out over 30 min. We assume that the reason for this is the rapid increase in free nickel sites, since most of them are occupied by hydrogen under methanation conditions. Because more nickel sites are available, more CO can adsorb, even when the gas phase concentration is lower. However, this is an educated guess at this point, and more detailed investigations are needed in future work to support this hypothesis.

In the simulation of the CO_2:H_2 inlet ratio change from 1:4 to 1:1 and vice versa (Figures 5e,f), the change in formate and Ni-CO is well described. For the simulation of the step 1:4 to 1:1, formate exhibits a peak in the transition area, which could be explained by an CO_2 to H_2 ratio favorable for formate formation. Possible reasons why this effect is not observed in the DRIFTS measurements are the same than for the H_2 drop in and drop out experiments. For the feed ratio change of 1:4 to 1:8 (Figure 5g,h) and vice versa, the RAS-5 model predicts the overall trend of Ni-CO and formate correctly. As a side note, the DRIFTS measurements (see Figures 3g,h) indicate that the formate concentration is almost constant during these experiments. Thus, it can be concluded that the pronounced gradients only stem from the normalization of the data needed for the qualitative comparison to the simulation results.

The simulation of SV variation experiments (Figure 5i,j) shows the same trends as the experimental data for formate. However, for Ni-CO, the trends are not correctly predicted. In the simulations, higher flow rates result in higher CO and Ni-CO concentrations, as a result of the overall lower conversion. In the experimental data, hardly any clear trend can be observed. Further results for the simulated surface coverages in different reaction zones are displayed in Figure S6 in the supporting information.

While the RAS-5 model and the LHHW model are in good agreement with each other for all experiments for the here investigated setup and conditions, the model prediction diverges from the experimental data for adsorbed carbon monoxide during complete H_2 drop outs. Furthermore, the gradients in the surface species are underestimated for some experiments. Nevertheless, the RAS-5 model shows clear potential in describing surface reactions that are not in equilibrium, and which therefore cannot be described by Langmuir–Hinshelwood-type models. At the current state, some factors are still limiting the further refinement of these models. The parameter estimation routine needs to be extended to include weighted steady-state and dynamic data, which is currently limited by computational restrictions, especially regarding the handling and processing of the huge amount of measurement data resulting from the DRIFTS experiments, in total approx. 29,400 data points were collected. The experimental setup needs to be further investigated, and the exact residence time distribution under all relevant conditions has to be measured to develop a sound numerical model. The correlation of the DRIFTS signal with temperature and the surface coverages of the respective species should be further investigated. These aspects offer various opportunities for refining the presented approach in future research.

4 | Summary and Conclusion

The objective of the authors' joint project within the priority program SPP2080 "DynaKat" of the German Research Foundation was to investigate effects on the catalyst surface during dynamic methanation, make them measurable, and derive reaction kinetic models of adequate complexity to be used in reactor modeling and optimization.

For this, an innovative laboratory reactor (denoted as spatially resolved DRIFTS (SRD) reactor) was developed, built, commissioned, and applied within the consortium's subproject "Spatial and temporal resolved operando analysis of methanation catalysts under transient and deactivating operating conditions" at KIT [19]. As a unique feature, this reactor combines GC sampling at four different positions along the reaction zone and allows spatially and temporally resolved optical investigation using *operando* DRIFTS of the methanation catalyst surface, which was applied via screen printing onto metallic catalyst support foils, which represents the five consecutive reaction zones investigated. These features allow to link gas phase concentrations with surface absorbance data. To prove the comprehensive applicability of the design, a Ni/Al_2O_3 catalyst, referred to as SPP2080-IMRC, which served as an industrial methanation reference catalyst within the SPP2080 consortium, was used. The catalyst was investigated in various steady-state and dynamic experiments, and a database for kinetic modeling was established.

The dynamic experiments in the SRD reactor allowed further insight into the reaction system of the CO_2 methanation. A data set of 210 experiments were carried out, investigating the dynamically operated methanation reaction in a custom-made spatially resolved DRIFTS reactor. Gaseous CO_2 and CH_4, and adsorbed formate and Ni-CO were investigated under transient operation conditions as well as a function of temperature and location in the reactor. The CO_2 drop out experiments clearly show that the surface concentrations of formate and Ni-CO are in direct dependency on the partial pressure of CO_2. The H_2 drop out shows the correlation between formate and Ni-CO, as for the dissociation of formate to Ni-CO, no H_2 is needed, leading to a decrease in the formate concentration and an increase in the concentration of Ni-CO. By varying the feed composition, the signals of the adsorbed species follow the partial pressure of CO_2, while formate shows a stronger dependency as it is formed before Ni-CO. The variation of the SV showed that the formate concentration varies strongly with the conversion of CO_2, while Ni-CO stays rather constant during the experiment.

A kinetic model was derived within the subproject "Methods and models for deriving optimal operations policies for dynamic methanation from model-based optimization and kinetic measurements" at TU Dortmund University and parametrized using the steady-state experimental data. The model shows good agreement with the experimental gas phase data gathered from steady state experiments with a GC, while featuring signs of overfitting from a statistical analysis point of view, such as standard deviations in the order of magnitude of the value itself. As a consequence, gas phase data alone is not sufficient to parametrize the postulated models, which

further proves the necessity and value of the SRD reactor setup.

The laboratory plant of the SRD reactor setup was modeled using an approach of a combination of piping with laminar flow and axial dispersion representing the reactor's periphery, and a one-dimensional reactor model also considering axial dispersion. With the RAS-5 kinetic model and the LHHW model, the concentrations of CO_2 and CH_4 in the gas phase can be described reasonably well. It has been shown that, in contrast to the LHHW kinetics, the RAS kinetic model is capable of describing the delayed response of surface species for most experiments and can be adjusted using experimental data. It has to be noted that the absolute values cannot be validated since the quantitative relation between absorbance in DRIFTS and the surface concentration of the species is not known. Further investigations on the molar uptake capacity of the catalyst within the SRD reactor are necessary, as well as the development of a procedure to calibrate the DRIFTS data to allow for a more quantitative interpretation of the measured data. Different adaptations to the laboratory plant can offer the possibility to further separate residence time effects from kinetic effects and thereby further improve the quality of the data. To conclude, in this work, a first-of-its-kind procedure for utilizing *operando* DRIFTS data on surface species for parameter estimation was elaborated, and its use for deriving and parameterizing high-fidelity reaction kinetic models is demonstrated.

Author Contributions

David Kellermann: conceptualization, data curation, formal analysis, investigation, methodology, software, validation, visualization, writing – original draft. **Timo Engl**: data curation, formal analysis, investigation, methodology, visualization, writing – original draft. **Lukas Lipinski**: software, validation. **Roland Dittmeyer**: resources, writing – review & editing, supervision. **Michael Rubin**: conceptualization, funding acquisition, project administration, supervision, visualization, writing – review & editing. **Hannsjörg Freund**: conceptualization, funding acquisition, project administration, resources, supervision, visualization, writing – review & editing.

Acknowledgments

The authors acknowledge funding by the German Research Foundation (DFG) within the priority program SPP2080 "DynaKat" (KL 3223/1-1/-2 and FR 2918/3-1/-2). The authors would also like to thank Prof. T. Franken and Dennis Weber (Technical University of Darmstadt) and the whole SPP2080 consortium for the fruitful discussions.

Open access funding enabled and organized by Projekt DEAL.

Conflicts of Interest

The authors declare no conflicts of interest.

Data Availability Statement

The data that support the findings of this study are available from the corresponding author upon reasonable request.

References

1. M. Langer, D. Kellermann, and H. Freund, "Kinetic Modeling of Dynamically Operated Heterogeneously Catalyzed Reactions: Microkinetic Model Reduction and Semi-mechanistic Approach on the Example of the CO_2 Methanation," *Chemical Engineering Journal* 467 (2023): 143217, https://doi.org/10.1016/j.cej.2023.143217.

2. S. Rönsch, J. Schneider, S. Matthischke, et al., "Review on Methanation—From Fundamentals to Current Projects"," *Fuel* 166 (2016): 276–296, https://doi.org/10.1016/j.fuel.2015.10.111.

3. M. Tommasi, S. N. Degerli, G. Ramis, and I. Rossetti, "Comprehensive Review of Catalysis, Reactor Design and Process Optimization," *Chemical Engineering Research and Design* 201 (2024): 457–482, https://doi.org/10.1016/j.cherd.2023.11.060.

4. J. Gorre, F. Ruoss, H. Karjunen, J. Schaffert, and T. Tynjälä, "Cost Benefits of Optimizing Hydrogen Storage and Methanation Capacities for Power-to-Gas Plants in Dynamic Operation," *Applied Energy* 257 (2020): 113967, https://doi.org/10.1016/j.apenergy.2019.113967.

5. K. L. Fischer, M. R. Langer, and H. Freund, "Dynamic Carbon Dioxide Methanation in a Wall-Cooled Fixed Bed Reactor: Comparative Evaluation of Reactor Models," *Industrial & Engineering Chemistry Research* 58 (2019): 19406–19420, https://doi.org/10.1021/acs.iecr.9b02863.

6. S. Rönsch, J. Köchermann, J. Schneider, and S. Matthischke, "Global Reaction Kinetics of CO and CO_2 Methanation for Dynamic Process Modeling," *Chemical Engineering & Technology* 39 (2016): 208–218, https://doi.org/10.1002/ceat.201500327.

7. F. Koschany, D. Schlereth, and O. Hinrichsen, "On the Kinetics of the Methanation of Carbon Dioxide on Coprecipitated NiAl(O)," *Applied Catalysis B: Environmental* 181 (2016): 504–516, https://doi.org/10.1016/j.apcatb.2015.07.026.

8. J. Xu and G. F. Froment, "Methane Steam Reforming, Methanation and Water-Gas Shift: I. Intrinsic Kinetics," *AIChE Journal* 35 (1989): 88–96, https://doi.org/10.1002/aic.690350109.

9. B. Kreitz, J. Friedland, R. Güttel, G. D. Wehinger, and T. Turek, "Dynamic Methanation of CO_2–Effect of Concentration Forcing"," *Chemie Ingenieur Technik* 91 (2019): 576–582, https://doi.org/10.1002/cite.201800191.

10. J. Friedland, T. Turek, and R. Güttel, "Investigations on the Low Temperature Methanation With Pulse Reaction of CO," *Chemie Ingenieur Technik* 88 (2016): 1833–1838, https://doi.org/10.1002/cite.201600056.

11. J. Friedland and R. Güttel, "Linking Gas-Phase Balance and Processes at the Solid Catalyst Surface With Pulse Series Method," *ChemCatChem* 14 (2022): e202200298, https://doi.org/10.1002/cctc.202200298.

12. J. Friedland, T. Turek, and R. Güttel, "Study on the Tolerance of Low-Temperature CO Methanation With Single Pulse Experiments," *Chemical Engineering Journal* 443 (2022): 136262, https://doi.org/10.1016/j.cej.2022.136262.

13. D. Meyer, J. Friedland, J. Schumacher, and R. Güttel, "The Periodic Transient Kinetics Method for Investigation of Kinetic Process Dynamics Under Realistic Conditions: Methanation as an Example," *Chemical Engineering Research and Design* 173 (2021): 253–266, https://doi.org/10.1016/j.cherd.2021.07.011.

14. D. Meyer, J. Friedland, J. Schumacher, M. G. Gäßler, and R. Güttel, "Hydrogenation of CO/CO_2 Mixtures Under Unsteady-state Conditions: Effect of the Carbon Oxides on the Dynamic Methanation Process," *Chemical Engineering Science* 250 (2022): 117405, https://doi.org/10.1016/j.ces.2021.117405.

15. D. Meyer, J. Schumacher, J. Friedland, and R. Güttel, "Frequency Response Analysis of the Unsteady-State CO/CO_2 Methanation Reaction: An Experimental Study," *Industrial & Engineering Chemistry Research* 61 (2022): 2045–2054, https://doi.org/10.1021/acs.iecr.1c04547.

16. J. Kopyscinski, T. J. Schildhauer, F. Vogel, S. M. Biollaz, and A. Wokaun, "Applying Spatially Resolved Concentration and Temperature Measurements in a Catalytic Plate Reactor for the Kinetic Study of CO Methanation," *Journal of Catalysis* 271 (2010): 262–279, https://doi.org/10.1016/j.jcat.2010.02.008.

17. J. A. Hernandez Lalinde, K. Kofler, X. Huang, and J. Kopyscinski, "Improved Kinetic Data Acquisition Using an Optically Accessible Catalytic Plate Reactor With Spatially-Resolved Measurement Techniques. Case of Study: CO_2 Methanation," *Catalysts* 8 (2018): 86, https://doi.org/10.3390/catal8020086.

18. J. A. Hernandez Lalinde, P. Roongruangsree, J. Ilsemann, M. Bäumer, and J. Kopyscinski, "CO_2 methanation and Reverse Water Gas Shift Reaction. Kinetic Study Based on In Situ Spatially-resolved Measurements," *Chemical Engineering Journal* 390 (2020): 124629, https://doi.org/10.1016/j.cej.2020.124629.

19. T. Engl, M. Langer, H. Freund, M. Rubin, and R. Dittmeyer, "Tap Reactor for Temporally and Spatially Resolved Analysis of the CO_2 Methanation Reaction," *Chemie Ingenieur Technik* 95 (2023): 658–667, https://doi.org/10.1002/cite.202200204.

20. D. Weber, T. Engl, M. Raabe, et al., "Revealing the Characteristics of Supported Ni-Mn Based Mixed Metal Oxide Catalysts: Operando Insights Into Their Activation and CO_2 Methanation Behavior," *Applied Catalysis A: General* 708 (2025): 120582, https://doi.org/10.1016/j.apcata.2025.120582.

21. S. Sichert, S.-F. Stahl, O. Korup, and R. Horn, "Measuring Adsorbate Profiles in Heterogeneous Catalytic Reactors by Iso-Potential Operando DRIFTS Applied to CO_2 Methanation on Ni," *ACS Catalysis* 14 (2024): 8676–8693, https://doi.org/10.1021/acscatal.4c00536.

22. D. Schmider, L. Maier, and O. Deutschmann, "Reaction Kinetics of CO and CO_2 Methanation Over Nickel," *Industrial & Engineering Chemistry Research* 60 (2021): 5792–5805, https://doi.org/10.1021/acs.iecr.1c00389.

23. National Institute of Standards and Technology, *NIST-JANAF Thermochemical Tables*, 4th ed. (American Institute of Physics, 1998).

24. T. Engl, D. Kellermann, J. Kopyscinski, H. Freund, M. Rubin, and R. Dittmeyer, "Spatially Resolved Operando Investigations of the CO_2 Methanation Reaction Using DRIFTS and Gas Phase Analysis submitted, Fuel," (2026).

25. S. Weber, R. T. Zimmermann, J. Bremer, et al., "Digitization in Catalysis Research: Towards a Holistic Description of a Ni/Al_2O_3 Reference Catalyst for CO_2 Methanation," *ChemCatChem* 14 (2022): e202101878, https://doi.org/10.1002/cctc.202101878.

26. S. Weber, K. L. Abel, R. T. Zimmermann, et al., "Porosity and Structure of Hierarchically Porous Ni/Al_2O_3 Catalysts for CO_2 Methanation," *Catalysts* 10 (1471): 1471, https://doi.org/10.3390/catal10121471.

27. L. Falbo, C. G. Visconti, L. Lietti, and J. Szanyi, "Combined Steady-State Reactivity and Transient DRIFT Spectroscopy Study," *Applied Catalysis B: Environmental* 256 (2019): 117791, https://doi.org/10.1016/j.apcatb.2019.117791.

28. L. Proaño, E. Tello, M. A. Arellano-Trevino, S. Wang, R. J. Farrauto, and M. Cobo, "In-Situ DRIFTS Study of Two-Step CO_2 Capture and Catalytic Methanation Over Ru,"Na_2O"/Al_2O_3 Dual Functional Material," *Applied Surface Science* 479 (2019): 25–30, https://doi.org/10.1016/j.apsusc.2019.01.281.

29. N. Schreiter, J. Kirchner, and S. Kureti, "A DRIFTS and TPD Study on the Methanation of CO_2 on Ni/Al_2O_3 Catalyst," *Catalysis Communications* 140 (2020): 105988, https://doi.org/10.1016/j.catcom.2020.105988.

30. M. Langer and H. Freund, "Reaction Kinetic Modeling of the CO X Methanation Over a Broad Range of Operation Conditions on an Impregnated Ni/Al_2O_3 Catalyst," *Industrial & Engineering Chemistry Research* 63 (2024): 10981–10996, https://doi.org/10.1021/acs.iecr.4c00819.

31. O. Levenspiel, *The Chemical Reactor Omnibook* (OSU Book Stores, 2002).

32. M. Kleiber and R. Joh, *VDI-Wärmeatlas* (Springer, 2013).

33. D. F. Fairbanks and C. R. Wilke, "Diffusion Coefficients in Multicomponent Gas Mixtures," *Industrial & Engineering Chemistry* 42 (1950): 471–475, https://doi.org/10.1021/ie50483a022.

34. X. Wang, H. Shi, J. H. Kwak, and J. Szanyi, "Mechanism of CO_2 Hydrogenation on Pd/Al_2O_3 Catalysts: Kinetics and Transient DRIFTS-MS Studies," *ACS Catalysis* 5 (2015): 6337–6349, https://doi.org/10.1021/acscatal.5b01464.

Supporting Information

Additional supporting information can be found online in the Supporting Information section.

Data supporting the findings of this study, additional information on the modeling and notation, are given in the Supporting Information.

The authors have cited additional references within the Supporting Information [25, 30].

Supporting File: cctc70765-sup-0001-SuppMat.pdf.